

# Chapter 16

## Development of a CFD Model for the Estimation of Windage Losses Inside the Narrow Air Gap of an Enclosed High-Speed Flywheel



**Mahmoud Eltaweel, Christos Kalyvas, Yong Chen,  
and Mohammad Reza Herfatmanesh**

**Abstract** Concerns over global warming and the need to reduce carbon emissions have prompted the development of novel energy recovery systems. During urban driving, a significant amount of energy is lost due to continuous braking, which can be recovered and stored. The flywheel energy storage system can efficiently recover and store the vehicle's kinetic energy during deceleration. In this study, a Computational Fluid Dynamics (CFD) model was developed to assess the impact of air gap size, and rotor cavity pressure environment on the aerodynamic performance of an enclosed non-ventilated flywheel energy recovery system. Consequently, the flywheel rotor skin friction coefficients for various air gap sizes have been numerically determined to predict the windage losses over a wide operating range. The presented study aims to identify a correlation that accurately fits the rotor skin friction coefficients for a range of air gap sizes and operating conditions. Model validation was carried out to assess the validity of the CFD results, which showed good agreement between numerical and experimental data. The results demonstrated that the increase in the air gap size can lead to up to a 19% reduction in the windage loss depending on the operating speed of the flywheel, while the windage loss can be reduced by 33% when the operating pressure is reduced to 500 mbar. Windage losses can be reduced by 45% when the airgap size is greatest, and the operating pressure is lowest.

**Keywords** Energy recovery system · Mechanical storage · Taylor-Couette flow · Skin friction coefficient

---

M. Eltaweel (✉) · C. Kalyvas · Y. Chen · M. R. Herfatmanesh  
School of Physics, Engineering and Computer Science, University of Hertfordshire, Hatfield,  
Hertfordshire AL10 9AB, England  
e-mail: [m-eltaweel@outlook.com](mailto:m-eltaweel@outlook.com)

## 16.1 Introduction

Flywheel energy storage systems (FESS) are mechanical energy storage devices that use the moment of inertia of a rotating disc to store mechanical energy. By speeding or decelerating the flywheel rotor with an electric motor, generator, or Continuous Variable Transmission (CVT), energy can be provided to or withdrawn from the flywheel. FESS is designed for short-term energy storage, which is ideal for fault protection, peak shaving, frequency management, and vehicles. The optimal design for the flywheel rotor in FESS can improve energy storage performance while also lowering the cost of the system, making it a more commercially feasible energy storage solution [1].

The performance of a FESS can be influenced by rotor design parameters such as material, operating speed, overall size, topology, and shape. These affect the FESS's energy capacity by determining the moment of inertia and allowing for a uniform stress distribution. The total stored energy is influenced by the operating speed. The yield strength and density of the rotor material determine the maximum permitted stress and mass of the flywheel rotor, which in turn affect the maximum allowable stress of the flywheel rotor. To create an optimum flywheel for a given application, the rotor design and operating speed of the flywheel must be tuned [2]. The total standby losses, which contribute to self-discharge and might affect the FESS's overall efficiency, are influenced by the operating speed and rotor shape. Mechanical losses due to bearing friction and windage are the main causes of standby power losses. To assess standby losses, as well as run-time losses that occur while charging or discharging the FESS, literature studies have employed simulations based on analytical models [3] and empirical models based on experiments [4].

Gurumurthy et al. [5] used an experimental flywheel system at atmospheric pressure to measure the mechanical and electrical losses in the FESS. They increased the rotational speed of the FESS to 15,000 rpm and then allowed it to decelerate in various load and no-load scenarios. Mechanical losses, particularly drag losses, dominated power losses in their studies, accounting for 72% of total power losses at very high speeds. Skinner [4] investigated the mechanical and no-load electrical losses caused by the rotor's self-discharge during standby using a cylindrical composite rotor FESS accelerated to speeds of up to 5000 rpm. Mechanical losses were significantly affected by the running speed and vacuum pressure inside the FESS enclosure. Amiryar and Pullen [3] used analytical and empirical methods to calculate the windage and bearing friction losses in a cylindrical steel flywheel running at various low pressures and speeds ranging from 10,000 to 20,000 rpm. While windage losses increased nonlinearly with running speed, they could be significantly reduced by adjusting the vacuum pressure and the space between the rotor and the enclosure. In contrast, air pressure had little effect on bearing losses, which can be attributed to speed-dependent and load-dependent loss components. Furthermore, as operating speed increased, speed-dependent losses increased significantly more than load-dependent losses. As a result,

the operating speeds selected during FESS design may have a significant impact on these losses. The previous study discovered that FESS design parameters such as vacuum pressure, air gap, and operation speed had a significant impact on overall system standby power losses.

To create ideal FESS rotors with improved energy storage properties, it is critical to understand the relationship between critical rotor design parameters such as rotor length, airgap size, speed, and pressure level [2]. The goal of this paper is to first determine the effects of simultaneously changing multiple design parameters, such as operating speed and airgap size, on the rotor shape optimization problem, and to see if such an approach can offer a significant improvement in the FESS's energy storage characteristics. This will allow for the investigation of a much larger portion of the rotor design space, resulting in improved optimal rotor designs. A few studies have shown an interest in calculating windage losses inside FESS with small air gaps. Almost all empirical equations for estimating windage losses are derived from experimental apparatus with properties that differ significantly from those of FESS [6, 7]. As a result, the primary goal is to create some realistic tools that will enable designers to account for windage losses in their designs. Then, in this study, a numerical approach based on CFD calculations is used to quantify windage losses inside narrow air gaps of high-speed FESS. A parametric study was carried out to characterise the influence of rotation speed, air gap geometry, and pressure levels. A correlation based on CFD data is provided for the estimation of the rotor skin friction coefficient for a wide range of operations.

## 16.2 Numerical Models

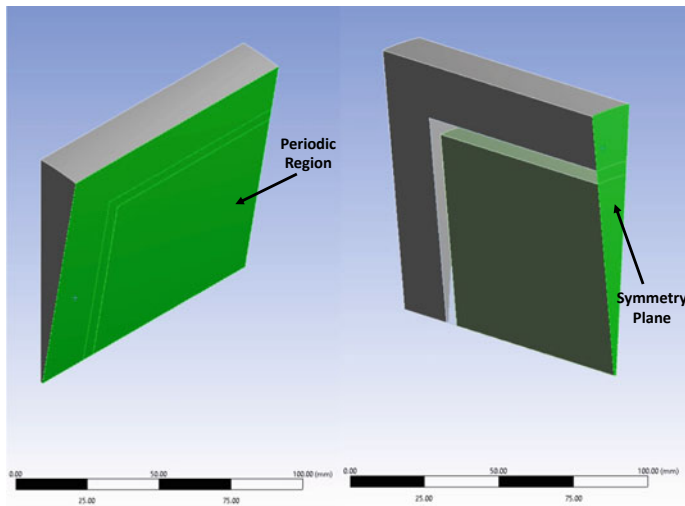
The current article suggests a numerical model of a smooth, narrow, and closed air gap. CFD methods are used to describe the air gap flow structure and predict the rotor skin friction coefficient. In order to estimate the skin friction coefficient, the air velocity distribution must be determined.

### 16.2.1 Mesh Generation and Boundary Conditions

The CFD programme used for this work is ANSYS Fluent 19.2 due to the improvement in the numerical analysis and its popularity in fluid and thermal analysis of complex designs. The parameter used in this study to define the airgap is a dimensionless parameter called the radius ratio which is  $\eta = R_i/R_o$  where  $R_i$  is the rotor radius and  $R_o$  is the internal housing radius. Another parameter is aspect ratio  $\Gamma = L/g$  where  $L$  is the rotor length and  $g$  is the airgap width ( $g = R_o - R_i$ ). The radius of the rotor was chosen to be 0.075 m. The values of the studied parameters are

**Table 16.1** Studied parameters values

Airgap $g$ (m)	0.0015	0.0048	0.0083
Radius ratio $\eta$	0.98	0.94	0.90
Rotor length $L$ (m)	0.1	0.15	0.2
Rotor cavity pressure (mbar)	1000	750	500

**Fig. 16.1** The simplified geometry of FESS with periodic region and symmetry plane

shown in Table 16.1. The allowable maximum rotational velocity for a solid cylinder rotor with a factor of safety of two was calculated to be 41,000 rpm when the rotor's material is steel 4340 [8].

The rotor and the housing walls are subjected to isothermal boundary conditions with an initial temperature of 24 °C. The FESS used in this investigation is shown in Fig. 16.1. To reduce the computational costs, the simulation was conducted on a 10°-slice from the FESS with a symmetry plane from the middle of it too.

### 16.2.2 Mesh Independence Analysis

Mesh independence analysis is essential before performing numerical analysis to select the appropriate mesh. A structured quadrilateral mesh is used in all of the airgap models in this study. The goal of this process is to find the best mesh that provides a solution independent of the mesh. To test the system, three different meshes were chosen. The airgap was 0.1–0.2 mm in size, and the rotor and housing were 1–2 mm in size. The average temperature of the air, rotor, and housing at a rotational speed of 40,000 rpm and atmospheric conditions were used for the independence

test. Figure 16.2 depicts the average temperature of the flywheel components for the three different meshes at different radius ratios. Mesh 2 was the most suitable mesh for this work for all radius ratios because the temperature of the airgap, rotor, and housing changed insignificantly between meshes 2 and 3. Further mesh refinement increases the computational time and costs of CFD modelling, making mesh 2 the best option. The inflation layers and the mesh used in the simulations are shown in Fig. 16.3.

CFD simulation was used to investigate the machine’s steady-state operation, as such steady-state models were used. Time-averaged steady-state solutions for the rotor’s relative motion are modelled using a moving reference frame (MRF). This method is appropriate for steady-state analysis and can resolve most flow characteristics such as mass flow rates and pressure rises and drops across the rotating components [9]. A turbulence model was required because the airgap had a Reynolds number in the turbulent region for all rotational velocities. Reynolds averaged Navier–Stokes (RANS) equations were solved using SST k-omega model. Based on a review of the existing literature for turbulence modelling of Taylor–Couette flow within concentric cylinders, the SST k-omega turbulence model is shown to be effective in estimating the fluid flow and heat transfer characteristics in concentric cylinders [10, 11]. The air was assumed to be an ideal gas and the viscosity was used under three equations sutherland and the effect of gravity was ignored. Thermal conductivity and specific heat were constant. The boundary conditions used in the solution are that the system

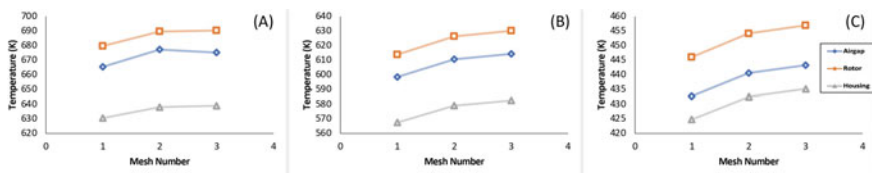


Fig. 16.2 Temperature values for the tested meshes for **a**  $\eta = 0.98$ , **b**  $\eta = 0.94$ , **c**  $\eta = 0.90$

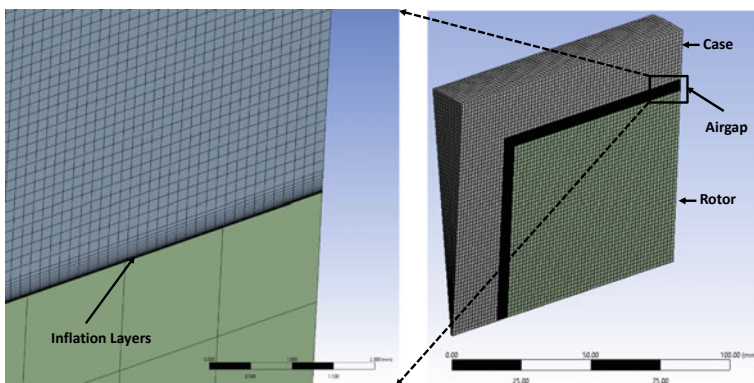


Fig. 16.3 The mesh used for the system

is closed with no inlet or outlet. The surfaces of the rotor and the housing are smooth with no-slip condition. Ambient temperatures of 24 °C and heat transfer coefficients of 30 W/m<sup>2</sup> K were used for the overall thermal boundary condition of the housing. The initial temperature for all the system components were selected to be 24 °C, room temperature. Wall treatment models were used to define the flow profiles in wall boundary layers because of the turbulence models' inability to accurately model the boundary layer regions affected by viscous effects. Near-wall flow velocities and distances are presented in the CFD section. The wall cell  $y_+ \leq 1$  was used to create a boundary layer mesh with a high resolution in order to resolve the viscous sublayer. Numerical discretization of the governing equations was carried out using a finite volume method to solve a linear algebraic equation system for each cell. The second-order upwind discretization scheme was used to simultaneously solve these problems based on mass, momentum, energy and turbulence parameter conservation. In order to ensure that the CFD solution is converged for each run, iterations were properly converged with respect to each other. The convergence criteria for all the residuals were set to be  $10^{-5}$  except for energy which was set at  $10^{-7}$ .

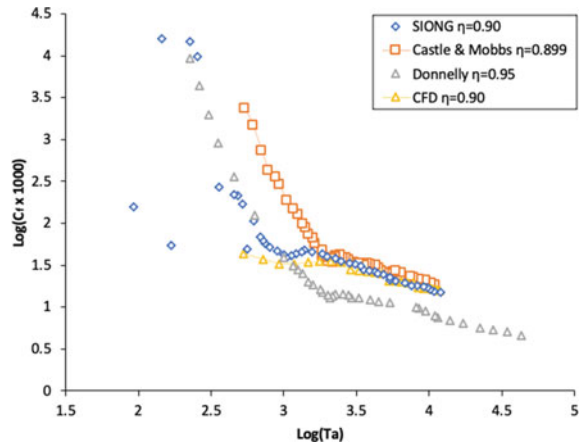
### 16.2.3 Validation

The skin friction coefficient variation as a function of Taylor number was compared to a number of experimental data points presented by Donnelly [12], Castle and Mobbs [13], and Siong [14], where the radius ratio was close enough to be compared with the experimental data. Figure 16.4 depicts the skin friction coefficient and Taylor number distributions. There are three distinct zones, the first of which is when the Taylor number is less than 1714 and the flow is laminar with no vortices, the second is a laminar flow with Taylor-Couette vortices, which can be referred to as non-linear theory due to the nonlinear aspect of the skin friction coefficient distribution, and the third zone is a turbulent flow in which the confined air is fully mixed. The numerically obtained critical Taylor numbers are in good agreement with the values proposed in the literature. Furthermore, when Taylor vortices form in the air gap, the skin friction coefficients estimated by CFD methods match well with Castle and Mobbs [13] and Siong [14], and the CFD calculations accurately reproduce the distribution of skin friction coefficients in the first zone. The predictions of the CFD model match the experimental data very well.

## 16.3 Results and Discussion

The effect of radius ratios on the skin friction coefficient for the rotor and disc sides of the flywheel at different rotational speeds is investigated. The outer cylinder (housing) is fixed. The inner cylinder (rotor) rotates at an angular velocity of 40,000 rpm, which is limited by the safety factor. The spike-shaped flow is caused by the creation of a

**Fig. 16.4** The variation between the skin friction coefficient of the rotor with respect to Taylor number



Taylor-Couette flow in the airgap. The air velocity closest to the housing is close to zero, while the velocity closest to the rotor is the greatest. A Taylor number critical value of 350 rpm can be obtained, indicating that the flow is not stable and Taylor vortices occur inside the airgap at all rotational speeds investigated. The intensity of the vortices increases as the rotational speed increases. Figure 16.5 represents the air velocity distribution plot for the Taylor vortices at the investigated rotational speeds. Within the air gap, Taylor vortices are symmetrical in the axial direction, where viscous forces are overcome by increasing rotational speed and inertial forces. The size of the Taylor vortex is affected by the speed of the rotor, where the vortices are reduced in terms of number at higher speeds, where the increase in rotational speed increases the distance between Taylor vortices.

Three rotor cavity pressure levels were investigated: 1000 mbar, 750 mbar, and 500 mbar. The rotor cavity pressure environment has little influence on the skin friction coefficient for both the rotor and disc surfaces; the only influencing parameter is the radius ratio with Taylor number, as shown in Fig. 16.6. While the effect is minor, lowering the pressure will result in a lower skin friction coefficient for both the rotor and the disc surfaces; however, the pressure will also lower the Taylor number under the same rotational velocity. Windage losses, on the other hand, are heavily influenced by rotor cavity pressure; lowering the pressure reduces windage losses, as illustrated in Fig. 16.7. For all radius ratios studied, the lowest pressure has the least windage losses, while the highest pressure has the most windage losses. Windage losses are significantly affected by pressure. The difference in total windage losses between 500 mbar for  $\eta = 0.98$  and 750 mbar for  $\eta = 0.90$  is less than 1%, making the choice of a larger airgap size with higher pressure a better solution in terms of complexity, because the lower the pressure, the more complex the vacuum system. Windage losses can be reduced by 16% and 33% for pressure environments of 750 mbar and 500 mbar, respectively, when compared to atmospheric pressure. Reducing the radius ratio from 0.99 to 0.94 and 0.90, on the other hand, can reduce total windage losses by 12% and 19%, respectively, under the three pressure environments studied.

When comparing  $\eta = 0.90$  and 500 mbar to  $\eta = 0.98$  and 1000 mbar, it is possible to achieve a 45% reduction in total windage losses, which could nearly double the standby time of a flywheel energy storage system.

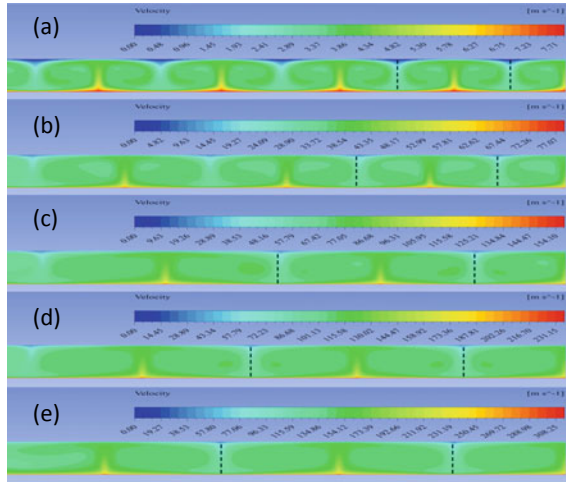


**Fig. 16.5** Air velocity distribution inside 0.90 radius ratio airgap for rotational speeds of (a) 1000 rpm, (b) 10,000 rpm, (c) 20,000 rpm, (d) 30,000 rpm, and (e) 40,000 rpm

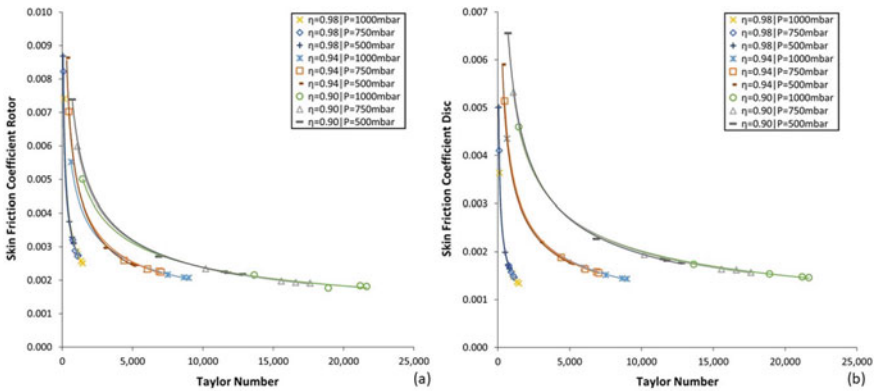
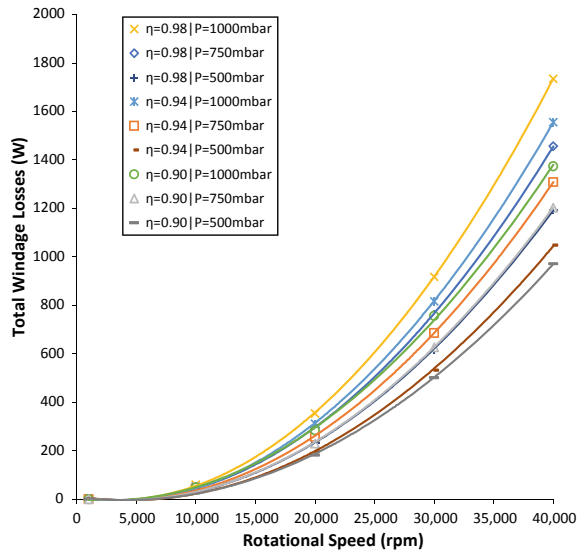


**Fig. 16.6** Taylor number for different radius ratios and pressure levels with skin friction coefficient for (a) rotor surface, and (b) disc surface

**Fig. 16.7** Variation of the total windage losses as a function of the rotational speed for three different pressure levels and radius ratios



### 16.3.1 Dimensionless Analysis

Based on the parametric study described above, a dimensionless analysis is performed to provide a piecewise expression of the rotor skin friction coefficient as a function of the studied parameters. The skin friction coefficient for the rotor and disc surfaces was expressed using two dimensionless parameters, the Reynolds number, and the radius ratio. This paper aims to establish new dimensionless parameter to better describe the skin friction coefficient for both the rotor and the disc surfaces for a pressure environment higher than 500 mbar. The proposed formulation is as follows:

$$C_{fr} = 0.3553 \times (1 - \eta)^{0.3} \times Re_r^{-0.4108} \tag{16.1}$$

$$C_{fd} = 0.4429 \times (1 - \eta)^{0.1} \times Re_d^{-0.4120} \tag{16.2}$$

where  $C_{fr}$  is the rotor skin friction coefficient,  $C_{fd}$  is the disc skin friction coefficient,  $Re_r$  is the Reynolds number between two concentric cylinders, and  $Re_d$  is the Reynolds number between a rotating disc and stationary wall.

### 16.4 Conclusion

Continuous braking causes a significant amount of energy to be lost while driving in cities, but this energy can be recovered and stored. The vehicle’s kinetic energy during deceleration can be effectively recovered and stored by the flywheel energy storage system. The aerodynamic performance of an enclosed non-ventilated flywheel energy

storage system was examined in this study using a computational fluid dynamics (CFD) model to determine the effect of air gap size, and rotor cavity pressure environment. In order to predict the windage losses over a broad operating range, the flywheel rotor skin friction coefficients for different scenarios have been numerically determined. Model validation was done to determine the validity of the CFD results, showing a good agreement between the numerical and experimental data. Based on the flywheel's operating speed, the results showed that increasing the air gap size can reduce windage loss by up to 19%, while lowering the operating pressure to 500 mbar can reduce windage loss by 33%. When the operating pressure is the lowest and the airgap size is the largest, windage losses can be reduced by 45%. A piecewise correlation was proposed for the estimation of the skin friction coefficient for the rotor and the disc surfaces for a variety of air gap sizes and operating circumstances.

**Acknowledgements** This work is supported by the European Union's Horizon 2020 research and innovation programme under the Marie Skłodowska-Curie grant agreement No 801604.

## References

1. A.K. Arani, H. Karami, G. Gharehpetian, M. Hejazi, Review of flywheel energy storage systems structures and applications in power systems and microgrids. *Renew. Sustain. Energy Rev.* **69**, 9–18 (2017)
2. V. Kale, M. Thomas, M. Secanell, On determining the optimal shape, speed, and size of metal flywheel rotors with maximum kinetic energy. *Struct. Multidiscip. Optim.* **64**(3), 1481–1499 (2021)
3. M.E. Amiryar, K.R. Pullen, Analysis of standby losses and charging cycles in flywheel energy storage systems. *Energies* **13**(17), 4441 (2020)
4. M.A. Skinner, Characterization of passive discharge losses in a flywheel energy storage system (2017)
5. S. Gurumurthy, A. Sharma, S. Sarkar, V. Agarwal, Apportioning and mitigation of losses in a flywheel energy storage system (2013), pp. 1–6
6. Y. Yamada, Torque resistance of a flow between rotating co-axial cylinders having axial flow. *Bull. JSME* **5**(20), 634–642 (1962)
7. E. Bilgen, R. Boulos, Functional dependence of torque coefficient of coaxial cylinders on gap width and Reynolds numbers (1973)
8. Y. Han, Z. Ren, Y. Tong, General design method of flywheel rotor for energy storage system, in *2012 International Conference on Future Energy, Environment, and Materials*, vol. 16 (2012), pp. 359–364. <http://doi.org/10.1016/j.egypro.2012.01.059>
9. J.D. Anderson, J. Wendt, *Computational Fluid Dynamics*, vol. 206 (Springer, Berlin, 1995)
10. A. Nachouane, A. Abdelli, G. Friedrich, S. Vivier, Estimation of windage losses inside very narrow air gaps of high speed electrical machines without an internal ventilation using CFD methods (2016), pp. 2704–2710
11. C. Jungreuthmayer et al., A detailed heat and fluid flow analysis of an internal permanent magnet synchronous machine by means of computational fluid dynamics. *IEEE Trans. Ind. Electron.* **59**(12), 4568–4578 (2011)

12. R. Donnelly, Experiments on the stability of viscous flow between rotating cylinders I. Torque measurements. Proc. R. Soc. Lond. Ser. Math. Phys. Sci. **246**(1246), 312–325 (1958)
13. P. Castle, F. Mobbs, Paper 6: hydrodynamic stability of the flow between eccentric rotating cylinders: visual observations and torque measurements, vol. 182, no. 14 (1967), pp. 41–52
14. L.S. Siong, An experimental investigation of Taylor Couette flow between eccentric cylinders (2007)

**Open Access** This chapter is licensed under the terms of the Creative Commons Attribution 4.0 International License (<http://creativecommons.org/licenses/by/4.0/>), which permits use, sharing, adaptation, distribution and reproduction in any medium or format, as long as you give appropriate credit to the original author(s) and the source, provide a link to the Creative Commons license and indicate if changes were made.

The images or other third party material in this chapter are included in the chapter's Creative Commons license, unless indicated otherwise in a credit line to the material. If material is not included in the chapter's Creative Commons license and your intended use is not permitted by statutory regulation or exceeds the permitted use, you will need to obtain permission directly from the copyright holder.

